communications earth & environment

A Nature Portfolio journal

Article

https://doi.org/10.1038/s43247-026-03437-8

# Divergent latitude-specific urban humid heat risks are regulated by local climate types

Check for updates

Lei Xu[1,4], Qiang Zhang[1] ✉, Senlin Tang[2,4], Xuhui Lee[3], Hongyu Song[1] & Xintong Gong[1]

Cities are home to more than half of the global population, and the urban heat island effect has aroused widespread concerns. Urban-induced changes in wet-bulb temperature and their health impacts remain less systematically investigated. Here we analyze the spatiotemporal evolution and drivers of wet-bulb temperature patterns across 56 globally representative cities during 2005-2024 using high-resolution reanalysis data. We find pronounced increases in global urban wet-bulb temperature since 2020, with spatially variable responses to urbanization and local climatic conditions. Tropical coastal cities such as Jakarta and Bangkok exhibit relatively stable and high wet-bulb temperature, where warm humid climate substantially offsets the urban heat island effect. In contrast, inland cities demonstrate pronounced spatial gradients. Metropolitan regions at low-to-mid latitudes display higher spatial heterogeneity than those at high latitudes. Mechanistic analysis reveals that variable responses of wet-bulb temperature to air temperature and relative humidity determine urbanization's influence. Extreme heat intensities reached remarkable levels during 2023-2024, posing serious health threats.

More than half of the global population resides in cities and projections indicate that urban demographics will surge from 56% in 2021 to 68% by 2050, approaching 70% by 2100[1]. Therefore, urban heat island (UHI) effects have emerged as a paramount global environmental concern[2,3] due to urbanization-induced elevated urban heat risks[4–8], and relevant urban inhabitants' health and thermal comfort[9–11]. Notably, in the backdrop of global warming, temperatures have risen approximately 1.1 °C above pre-industrial levels and are projected to reach the 1.5 °C threshold during 2030–2052[12]. The synergistic consequences of UHI effects and warming climate greatly amplify urban heat stress risks[13–15]. However, previous studies mostly focused on dry-bulb temperature variations[16–18], omitting humid heat stress, which impedes effective human thermoregulation mechanisms and pushes up health risks[2,19,20]. We hold the hypothesis that wet-bulb temperature-specific UHI may manifest different changing patterns when compared to dry-bulb temperature-specific UHI. Comprehensive understanding of wet-bulb temperature-specific UHI is critical in informing urban heat mitigation strategies and the protection of at-risk urban residents globally.

Wet-bulb temperature (Tw), which integrates air temperature and relative humidity, serves as a key bioclimatic measure. It reflects the lowest temperature attainable by evaporative cooling under specific environmental conditions and indicates the physiological threshold for human heat loss through sweating[21]. As a result, Tw has become the foremost metric for evaluating risks associated with humid heat stress[22]. The 2003 European heatwave, marked by concurrent extreme temperatures and high humidity, caused more than 70,000 fatalities, underscoring the severe public health risks associated with humid heat stress[9]. Under ongoing global warming, Tw has shown important increasing trends[2,23,24], particularly in climatically vulnerable regions, such as South Asia and the Middle East[3,19,25,26]. Several areas are now approaching the limits of human physiological tolerance[27,28], threatening the health and survival of billions of people. Urbanization further amplifies thermal risks through the UHI effect[29,30] and urban dry island (UDI) effect[31–35]. The relative strength of these phenomena influences the spatial variation in Tw between urban and rural zones. Although numerous studies have examined the impact of urbanization on Tw[2,36–38], comprehensive analyses of the spatiotemporal heterogeneity of Tw across cities with diverse local environmental backgrounds remain limited.

Recent investigations have importantly advanced our understanding of how urbanization influences Tw[2,36–38]. Notably, Zhang et al.[2] systematically uncovered the climate-dependent characteristics of urban wet-bulb island effects using global meteorological station data from urban and rural areas, providing a key scientific basis for assessing the compound impacts of

[1]School of Technology for Sustainability, Guangdong Provincial Key Laboratory of Wastewater Information Analysis and Early Warning, Beijing Normal University, Zhuhai, China. [2]School of Remote Sensing Science and Technology, Aerospace Information Technology University, Jinan, China. [3]School of the Environment, Yale University, New Haven, CT, USA. [4]These authors contributed equally this work: Lei Xu, Senlin Tang. ✉e-mail: zhangq68@bnu.edu.cn

urbanization on humid heat stress[2]. Nevertheless, persistent methodological limitations in this field constrain a mechanistic understanding of the complex interactions within urban thermal environments. First, prior studies have largely relied on subjectively selected urban and rural stations for comparative analyses. This approach, which uses subjective classification of meteorological stations to represent urban and rural conditions, lacks objective and consistent spatial criteria[5]. As a result, it fails to adequately capture the continuous gradient and spatial heterogeneity of urbanization[4]. Second, the sparse distribution and limited coverage of meteorological stations hinder a comprehensive characterization of humid heat patterns across diverse city types and regions. Critical areas, such as urban cores and peri-urban transition zones remain particularly undersampled. Furthermore, existing analyses focus predominantly on statistical descriptions of urban–rural Tw differences, with limited mechanistic insight into their sensitivity to key drivers, such as air temperature and relative humidity. This gap impedes a deeper understanding of the physical processes underlying urban–rural humidity and heat gradients. These limitations not only challenge the accuracy of early warnings for urban heat risks but also restrict the formulation of targeted adaptation strategies.

To address these knowledge gaps, we develop a comprehensive framework for assessing urban humid heat environments, grounded in objective spatial classification and multi-factor coupling analysis. This framework systematically elucidates the mechanisms through which urbanization influences Tw and its associated spatial differentiation patterns. This framework not only transcends the limitations of prior regional or single-factor analyses but also, for the first time, systematically assesses Tw dynamics across 56 representative global cities (2005–2024), revealing latitude-specific urban humid heat patterns and their underlying formation mechanisms. We particularly delve into the synergistic roles of temperature and water vapor pressure in shaping urban–rural Tw differentials, thereby filling critical gaps in comprehensively and cross-regionally assessing urban-specific humid heat vulnerabilities. Specifically, our study aims to address the following key scientific questions: (1) how do the spatiotemporal evolution patterns of Tw vary across global cities, and what are their heterogeneous characteristics? (2) What roles do temperature and water vapor pressure play in shaping the urban–rural differentials in Tw? (3) What are the distribution characteristics of humid heat events and population exposure risks at the global scale? By constructing long-term datasets from globally representative cities and leveraging the high spatiotemporal resolution of multi-source observational data, we apply urban–rural gradient analysis and multivariate sensitivity decomposition methods to systematically examine the compound regulatory effects of urbanization on humid heat environments. Our findings shed insights on urban climatology and human settlement science, providing foundational data for climate change adaptation assessments and policy development, and deliver a scientific basis for heat-risk identification, early warning systems, and adaptive planning across diverse urban contexts.

## Results

### Variable spatiotemporal patterns of Tw

The selected sample cities are predominantly distributed between 23.5°N and 66.5°N, with approximately 64% situated in low- to mid-latitudes and half of the total classified as inland (Fig. 1c). The Tw data were obtained from multi-source observations and show strong consistency with a global dataset derived from meteorological stations (Supplementary Fig. 1). We observe a pronounced latitudinal gradient in global urban Tw, with mean values declining from 26 °C in tropical regions to below −30 °C in polar cities (Fig. 1a). The highest Tw values are predominantly found in coastal cities across South Asia, Southeast Asia, and North Africa (Fig. 1b). In contrast, urban areas with Tw below 10 °C are largely confined to temperate and frigid zones north of 45°N (Fig. 1b). Standardized Tw anomalies at the city scale further support these spatially heterogeneous patterns. The highest standard deviations occur in low-latitude coastal cities (0.8–1.2), values approximately 2.3 times greater than those observed in high-latitude inland cities (0.3–0.6). This contrast underscores the pronounced influence of relative humidity on Tw under maritime climatic conditions (Supplementary Fig. 2).

During the period 2005–2024, global urban Tw showed a marked upward trend, with a particularly pronounced rise in both mean and maximum Tw after 2020 (Fig. 1d). At the city scale, approximately 80% of urban areas exhibited a high frequency of positive Tw anomalies after 2020. This was especially evident in tropical cities—such as Jakarta and Manila—as well as in subtropical cities including Paris and London (Supplementary Fig. 2). Tw has risen persistently since 2021, a trend statistically validated through linear regression analysis (see "Methods"), and reached a record high during 2023–2024 (Fig. 1e). Notably, the maximum Tw increased at a greater rate than the mean Tw (Supplementary Fig. 2). This asymmetric pattern is likely attributable to the exponential increase in atmospheric moisture-holding capacity under high-temperature conditions, as governed by the Clausius–Clapeyron relationship[39,40]. Such a mechanism renders extreme Tw values more sensitive to temperature changes than mean values, illustrating a nonlinear amplification effect within the climate system under extreme conditions.

Tw gradients reveal complex spatial patterns along urban-to-rural transects. Gradient analysis based on the relative brightness index (RBI) shows that standardized Tw indices in urban warming zones (regions where wet-bulb temperature increases with urban–rural gradient) increase progressively from 0.52 in rural regions to 0.72 in urban cores, illustrating characteristic UHI effects (Fig. 2a, b). In contrast, Tw indices in urban cooling zones (regions where wet-bulb temperature decreases with urban–rural gradient) decline from 0.45 in city centers to 0.35 in peri-urban transition areas, highlighting the moderating influence of urban vegetation and water bodies through evaporative cooling[36,41]. Approximately 60% of global cities exhibit urban warming effects, with the majority located in humid and semi-humid climatic zones; the remaining 40% demonstrate cooling effects, which are predominantly concentrated in arid regions (Supplementary Fig. 3).

Intra-urban spatial heterogeneity analysis further clarifies the distribution patterns of Tw at the city scale. Cross-sectional Tw variations across the sampled cities reveal that tropical coastal cities (e.g., Jakarta, Manila, and Bangkok) exhibit moderate to high variability (Supplementary Fig. 4), suggesting that maritime climates can substantially mitigate UHI effects. In contrast, inland cities, such as Beijing, Delhi, Cairo, and Tehran, show more pronounced spatial gradients (Supplementary Fig. 4), reflecting the regulatory roles of topography and urbanization levels on local Tw distribution. High-latitude cities (e.g., Yakutsk, Norilsk, and Vorkuta) not only display lower absolute Tw values but also exhibit relatively subdued intra-urban spatial variability. Conversely, metropolitan areas at mid-to-low latitudes, including Tokyo, Seoul, and Shanghai, are characterized by stronger spatial heterogeneity (Supplementary Fig. 4).

To further elucidate the spatial heterogeneity of surface UHI intensity (Tw) across different urban forms, cities were categorized into emerging, urbanized, and transitional types (Fig. 2c). Distinct patterns of Tw changes were observed among these categories. Emerging cities (e.g., Tokyo, Japan; Osaka, Japan) exhibited the most pronounced warming, with Tw difference (ΔTw) values ranging from 0.10 to 0.14 °C. In contrast, transitional and urbanized cities (e.g., Guangzhou, China; Hyderabad, India) showed more moderate changes, with ΔTw between 0.02 and 0.04 °C. Meanwhile, rural and compact cities (e.g., Yakutsk, Russia; Baghdad, Iraq) displayed minimal warming trends (Fig. 2d). These differential patterns in Tw are likely attributable to variations in urbanization stages, including the extent of impervious surface expansion, building density, and anthropogenic heat emissions. Rapid land-use changes in emerging cities appear to amplify urban–rural temperature differences, whereas the stable urban structures of mature cities help maintain relatively consistent thermal gradients.

### Drivers behind the spatial heterogeneity of Tw

Regulation of UHI effects by local climatic conditions, land–sea thermal contrast, and urbanization-induced restructuring of the surface energy balance has been identified as a primary driver of UHI modification[8,42,43].

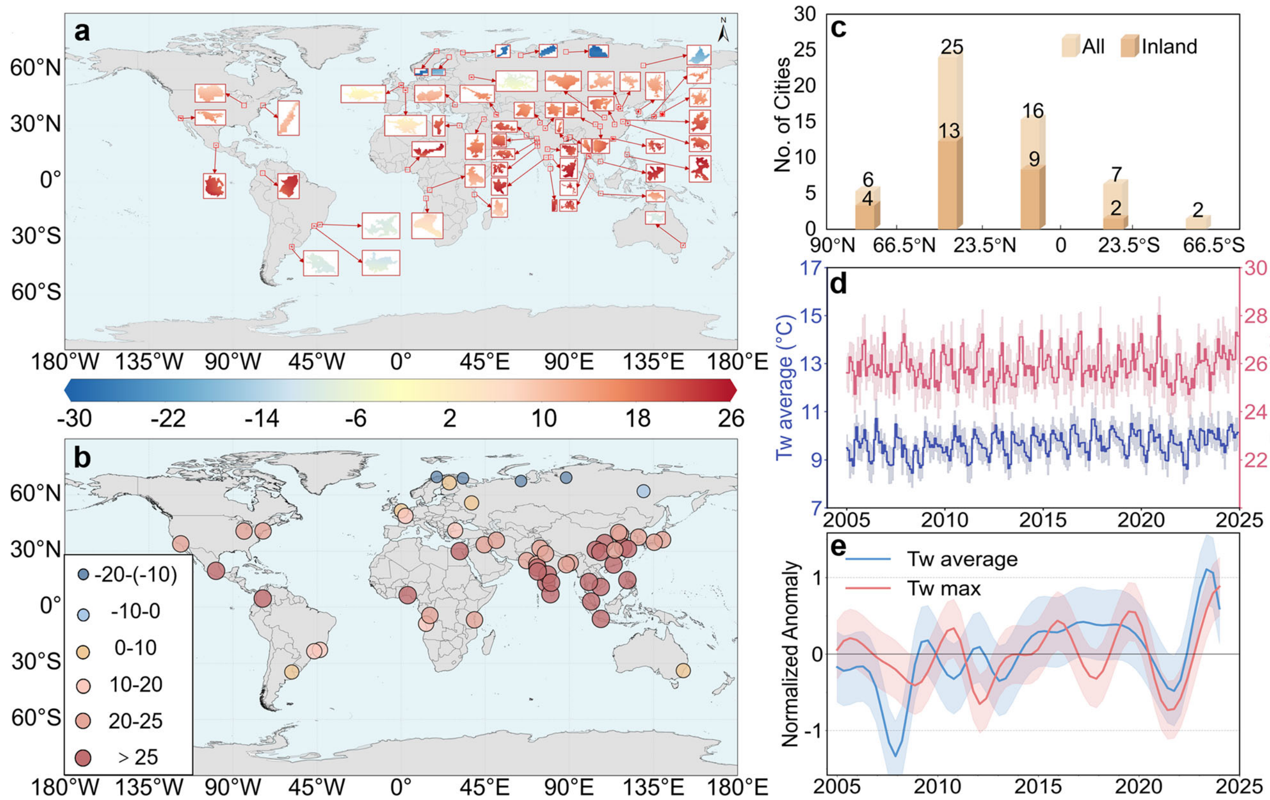


**Fig. 1 | Global patterns and temporal dynamics of Tw across cites.** **a** Multi-decadal mean Tw; **b** categorical maximum Tw; **c** latitudinal distribution of the analyzed cities; **d** temporal trends in mean and maximum Tw from 2005 to 2024; and **e** Temporal changes of the normalized Tw anomaly indices.

Accordingly, we selected climate type, distance from cities to the ocean, and level of urban development as potential key factors. Herein, a "dominant factor" is defined as a variable or condition that exerts the most substantial and primary influence on a particular phenomenon (e.g., urban–rural ΔTw differences), demonstrating a notably larger or more determinative impact compared to other contributing factors. Our analysis reveals that urban–rural differences in ΔTw are strongly modulated by these drivers. Climate type plays a dominant role, with cities in tropical zones exhibiting the most pronounced UHI effects. Inland tropical cities, for instance, show a mean annual ΔTw of 0.05 °C (Supplementary Fig. 5a). This enhancement is attributed to abundant atmospheric moisture, which improves the efficiency of sensible-to-latent heat conversion over urban surfaces, combined with low-albedo materials that promote substantial energy accumulation under intense solar radiation[44,45]. Conversely, polar climate zones display negative ΔTw values (Supplementary Fig. 5a), indicating higher rural than urban Tw. This reversal likely results from urban structures in polar regions reducing wind speed and inhibiting vertical turbulent mixing, thereby limiting heat and moisture exchange between the surface and atmosphere[46]. Additionally, urban surface materials in cold environments exhibit high thermal capacity and low thermal conductivity, further promoting UCI effects[47].

In tropical and arid climates, inland cities exhibit higher ΔTw compared to coastal cities (Supplementary Fig. 5a, c). In contrast, cities in temperate, continental, and polar zones show opposite Tw trends, with a polar coastal–inland ΔTw of 0.07 °C (Supplementary Fig. 5a, c). This pattern likely stems from the relatively stable temperature and humidity conditions in coastal cities during seasonal transitions, owing to the thermal inertia of mid- to high-latitude oceans[48]. Urbanization further disrupts land–sea thermal equilibrium and amplifies urban–rural Tw differences. Urban development levels also importantly shape ΔTw distributions. Emerging cities show the highest urban–rural ΔTw (Supplementary Fig. 5e), consistent with frequent extreme heat events driven by rapid land-use change and intensive construction during expansive urbanization[31,35]. In contrast, mature cities with stable development patterns exhibit smaller ΔTw. Distributions of ΔTw vary markedly across city types (Supplementary Fig. 5b, d, f). Tropical inland cities and emerging cities display particularly large standard deviations (Supplementary Fig. 5b, f), reflecting high variability and instability in urban–rural Tw differences.

To elucidate the physical mechanisms underlying urban–rural ΔTw and identify key drivers, we applied a decomposition analysis based on the Clausius–Clapeyron equation to partition Tw variations into independent contributions from temperature and water vapor pressure[39,40,49]. Notably, distinct spatial heterogeneity in temperature sensitivity and water vapor pressure sensitivity emerged at the global scale, governing the magnitude and sign of urbanization's effect on Tw. Water vapor pressure sensitivity peaked in low-latitude tropical and subtropical regions (0.8–1.0), with the Amazon and Congo basins exhibiting values exceeding 0.95 (Fig. 3a). In contrast, temperature sensitivity was strongest in mid-high latitudes—for instance, exceeding 0.7 across Northern Europe, Siberia, and northern North America, and reaching 0.85–0.90 along the margins of Greenland and Antarctica (Fig. 3b). The shallow slope of the saturation vapor pressure curve under cold conditions heightens the sensitivity of Tw to dry-bulb temperature changes. Normality of both sensitivity distributions was confirmed via Q–Q plots, with coefficients of determination of 0.9588 and 0.9592 for water vapor and temperature sensitivity, respectively. The maximum divergence between empirical and theoretical quantiles was 0.02, affirming the robustness and statistical validity of the sensitivity analysis (Supplementary Fig. 6).

Bivariate sensitivity analysis of spatial distribution characteristics identifies key physical criteria governing the influence of urbanization on Tw. In the two-dimensional space of water vapor pressure sensitivity versus temperature sensitivity, areas with $\Delta Tw > 0$ and $\Delta Tw \leq 0$ display clear clustering and separation (Fig. 3c). Quantitatively, regions where $\Delta Tw > 0$ show a mean water vapor pressure sensitivity of $0.62 \pm 0.18$, importantly higher than their mean temperature sensitivity ($0.36 \pm 0.15$), indicating that urban warming is primarily driven by changes in moisture availability. In contrast, regions with $\Delta Tw \leq 0$ exhibit higher temperature sensitivity

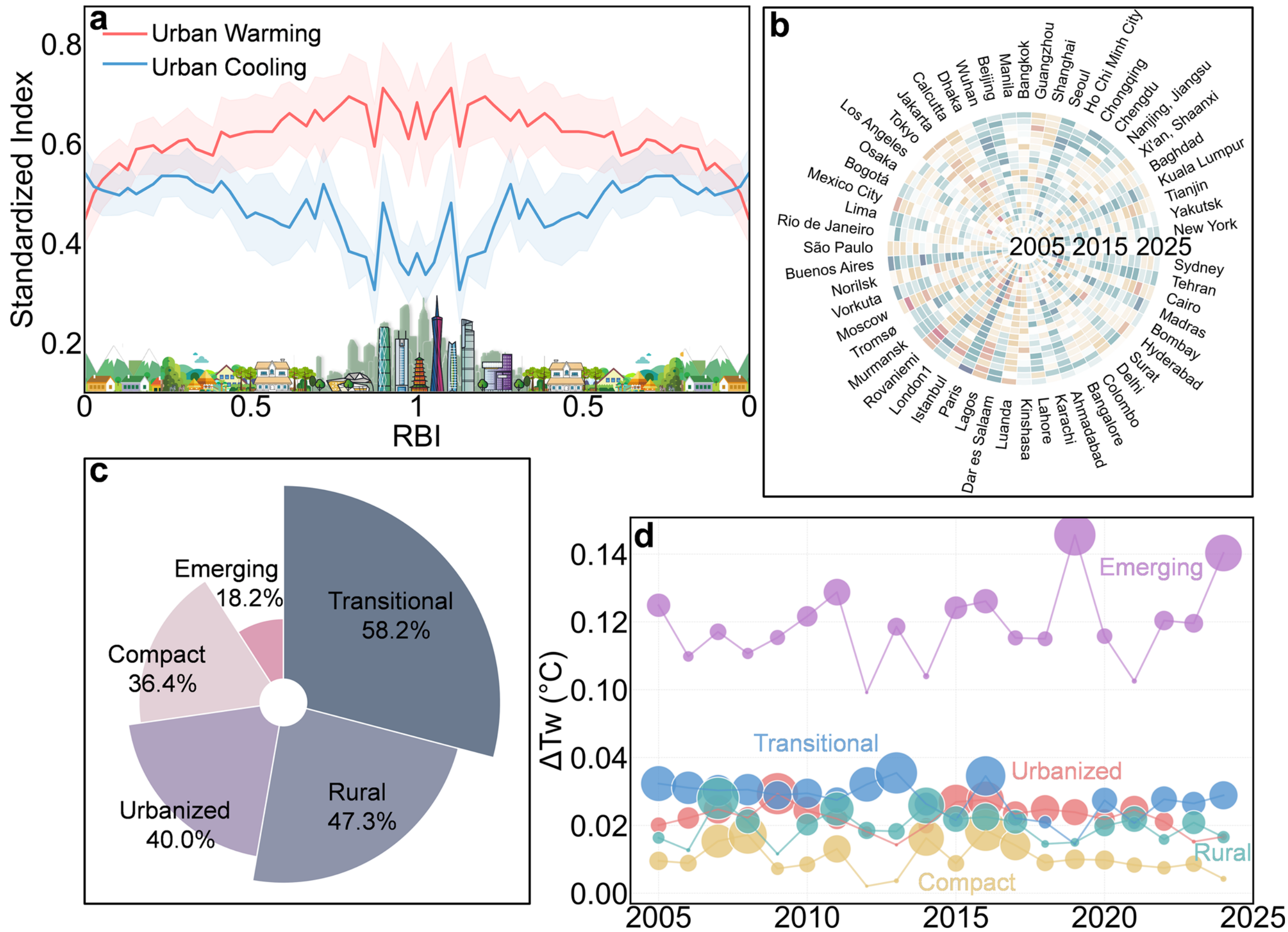


**Fig. 2 | Global patterns and trends of urban Tw for different city types.** **a** Variations in the standardized Tw index along the urban–rural gradient; **b** spatiotemporal changes in Tw across major global cities; **c** proportions of urban types within the study regions; **d** temporal trends in Tw increase by urban types. The data visualization was created by the authors using Python. The decorative cityscape elements were sourced from Microsoft PowerPoint's built-in graphics library (licensed to Beijing Normal University).

(0.55 ± 0.20) compared to water vapor pressure sensitivity (0.45 ± 0.17), suggesting that cooling zones are more responsive to thermal variations (Fig. 3d). The underlying mechanism for this divergence lies in how urbanization modifies surface evapotranspiration: in moisture-sensitive regions, urban–rural differences in humidity dominate Tw variations, whereas in thermally sensitive regions, differences in surface heat capacity and radiative balance play the leading role. Previous studies have largely examined thermal and moisture effects on urban Tw separately[16,27], limiting mechanistic understanding of their relative importance across diverse urban environments. Our bivariate sensitivity analysis provides the systematic framework to simultaneously quantify both mechanisms, revealing distinct spatial clustering patterns that offer crucial insights for predicting urbanization impacts on human thermal stress under climate change. Categorical sensitivity analysis further corroborates the mechanistic basis of these findings. Tropical zones exhibit dominant absolute humidity sensitivity, with inland and coastal cities recording values of 0.83 and 0.84, respectively. This elevated sensitivity arises from the full expression of the exponential saturated vapor pressure curve under near-saturated atmospheric conditions. In contrast, polar climates display the opposite pattern, with temperature sensitivity reaching 0.87–0.88. This reflects diminished temperature dependence of saturated vapor pressure under low temperatures (Supplementary Fig. 7), while land–sea modulation preserves climate-specific traits. Meanwhile, emerging cities show the highest vapor pressure sensitivity (0.74), indicating pronounced local humidity changes due to vegetation loss during urbanization. Highly urbanized cities exhibit sensitivity homogenization, signifying environmental stability in mature urban systems. These sensitivity patterns provide physical mechanistic evidence for the observed spatial variation in urban–rural ΔTw: the distribution of sensitivity types dictates the direction and magnitude of urbanization effects on Tw.

To elucidate how urban physical morphology regulates urban–rural ΔTw, we examined four key morphological characteristics: population density, vegetation coverage, urban area, and shape index. Urban area shows the strongest positive correlation with ΔTw ($R^2 = 0.546$, $p < 0.05$; Supplementary Fig. 8e), consistent with urban climate zonation theory[50] and established frameworks linking larger urban scales to heightened UHI intensity[51–53], likely due to enhanced thermal capacity and complex energy balances. Population density exhibits a important nonlinear positive correlation with ΔTw ($R^2 = 0.410$, $p < 0.05$; Supplementary Fig. 8a), reflecting the direct role of anthropogenic heat emissions and intensified human activities in amplifying local warming. Vegetation coverage shows no important correlation ($R^2 = 0.050$, $p \geq 0.05$; Supplementary Fig. 8c), suggesting that its cooling effects are offset by other urban factors and exhibit spatial heterogeneity (Supplementary Fig. 8d). The urban shape index is weakly positively correlated with ΔTw ($R^2 = 0.140$, $p < 0.05$; Supplementary Fig. 8g), indicating that irregular urban boundaries moderate heat exchange between urban and suburban areas[54]. Cluster analysis further confirms gradient differences in Tw responses across combinations of these morphological characteristics (Supplementary Fig. 8).

Multi-timescale analysis reveals strong seasonal coupling between the intensity of urban–rural ΔTw and its long-term trends. The correlation is most pronounced in summer ($r = 0.48$, $p < 0.05$; Supplementary Fig. 9b),

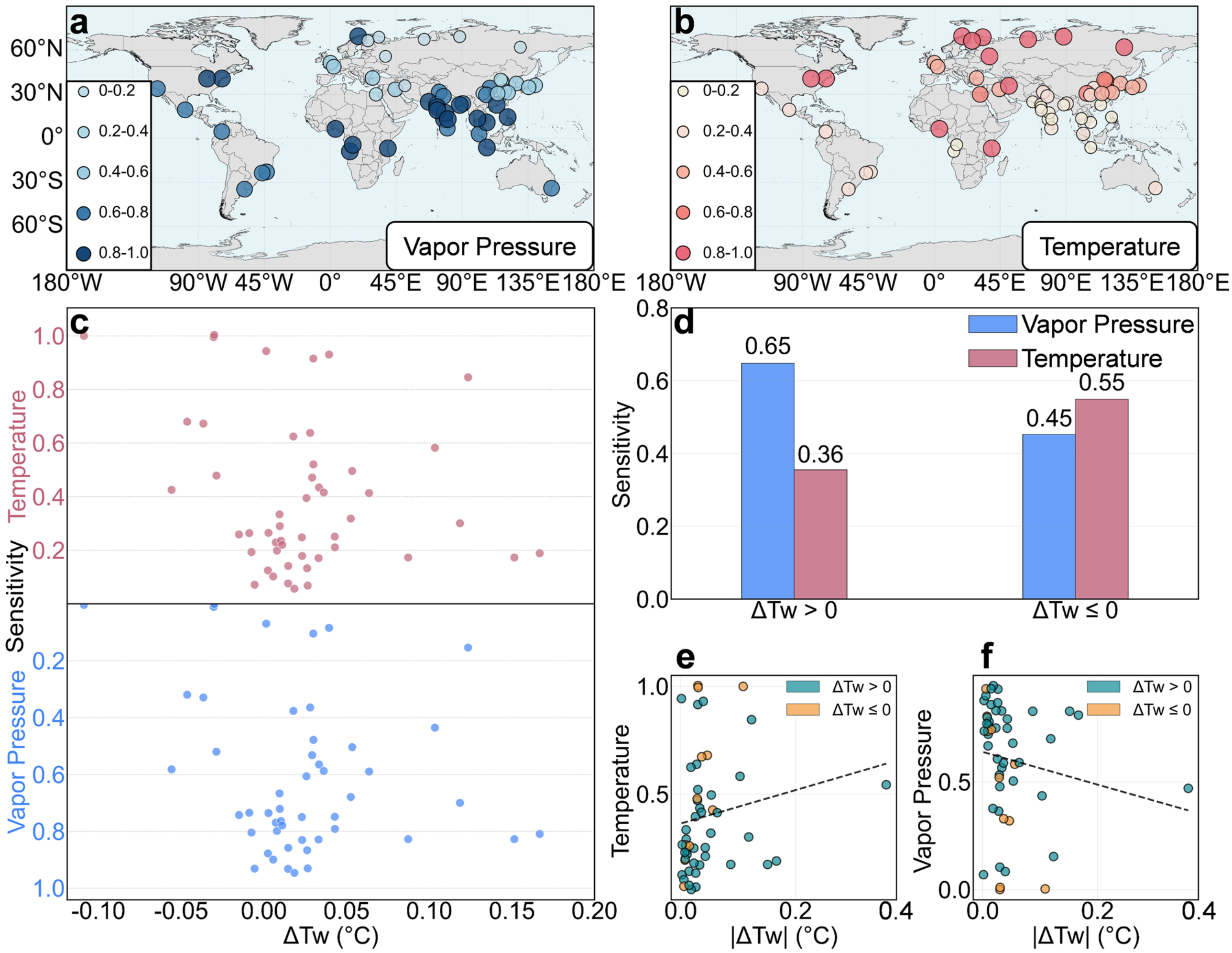


**Fig. 3 | Global sensitivity analysis of urban Tw. a** Spatial distribution of water vapor pressure sensitivity; **b** spatial distribution of temperature sensitivity; **c** bivariate relationship between sensitivities and urban–rural ΔTw; **d** comparison of mean sensitivities with different ΔTw sign groups; **e** relationship between temperature sensitivity and absolute urban–rural ΔTw; **f** relationship between water vapor pressure sensitivity and absolute urban–rural ΔTw. Circle sizes represent sensitivity magnitudes, and color intensity corresponds to sensitivity values.

suggesting that regions with intense urban humid heat effects also experience stronger long-term warming—consistent with heightened summer UHI activity and unstable boundary layer conditions[55]. The correlation weakens in winter ($r = 0.36$, $p < 0.05$; Supplementary Fig. 9c), reflecting seasonal modulation of UHI dynamics. The annual mean correlation is low ($r = 0.20$; Supplementary Fig. 9a), indicating that interannual averaging obscures important seasonal signals. After applying a 3–7-year moving average, correlations drop substantially ($r = 0.07$–$0.11$; Supplementary Fig. 9d–f), highlighting the importance of interannual variability in understanding long-term ΔTw evolution. A important positive correlation is also found between interannual variability and long-term trends ($r = 0.37$, $p < 0.05$; Supplementary Fig. 9h), implying that intrinsic fluctuations in urban humid heat systems contribute to long-term changes, with more variable regions showing stronger warming trends.

### Trends in humid heatwave events and population exposure

We further investigate the spatiotemporal heterogeneity of humid heat events, revealing their stratified and hierarchical risk structure. Based on the four levels of humid heat events defined above, we calculated the monthly average occurrence frequency for each event category and visualized them in the form of heatmaps. Mild events (Supplementary Fig. 10a) occur from June to September and intensify after 2020. Moderate events (Supplementary Fig. 10b) exhibit increased temporal clustering, primarily in July–August, with more spatially confined distributions and fluctuating yet rising annual frequencies since 2015. Severe events (Supplementary Fig. 10c) are further concentrated in the July–August core, showing relatively lower but more variable frequencies, notably with pronounced peaks during 2018–2020. Extreme events (Supplementary Fig. 10d) display the most constrained spatiotemporal patterns, with the lowest absolute frequencies yet the steepest recent increases, reaching the highest observed values in 2023–2024. This graded pattern indicates that higher-intensity events are increasingly concentrated in time and exhibit more distinct seasonal profiles. The marked upward trends in high-grade events underscore the escalating risks of extreme humid heat hazards under global warming.

We further identified clear temporal trends in the characteristics of humid-heat events. Analysis of event duration revealed that the most persistent heatwave within the study period occurred in 2023, lasting nearly 15 days—importantly longer than the historical average (Fig. 4a). Although this extreme duration is comparable to that of the 2008–2009 high-value period, the recent event was more intense. Similarly, the evolution of heat intensity showed that the peak value in 2024 approached 4 °C, setting a new record for the temporal series, while 2023 also exhibited marked intensification (Fig. 4b). More importantly, the cumulative heat index offers critical insight into the overall impact of these events (Fig. 4c). During both 2023 and 2024, the cumulative heat index exceeded 30 °C days, surpassing all

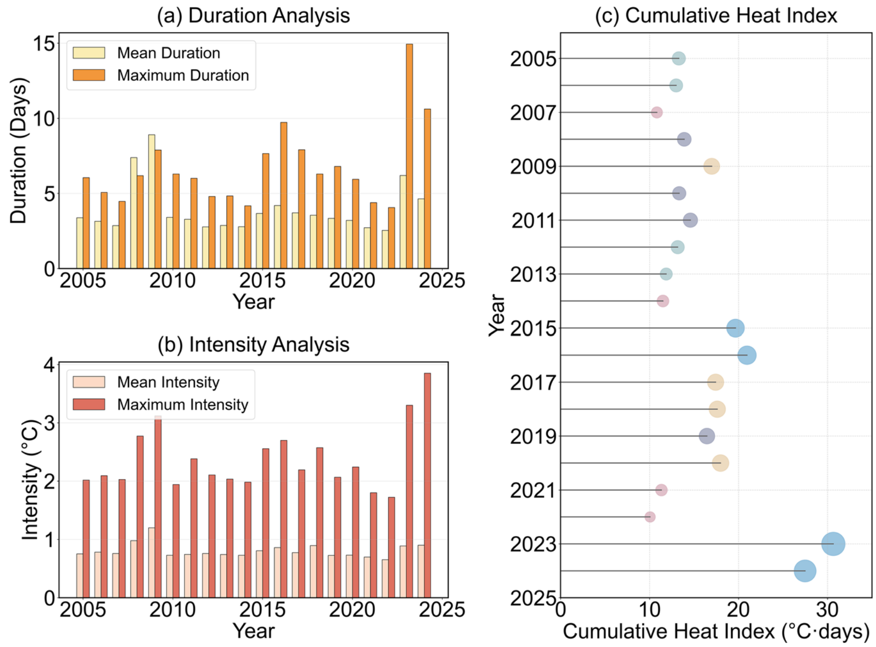


**Fig. 4 | Comprehensive analysis of heatwave event characteristic parameters (2005–2024).** **a** Duration analysis; **b** intensity analysis; **c** cumulative heat index distribution.

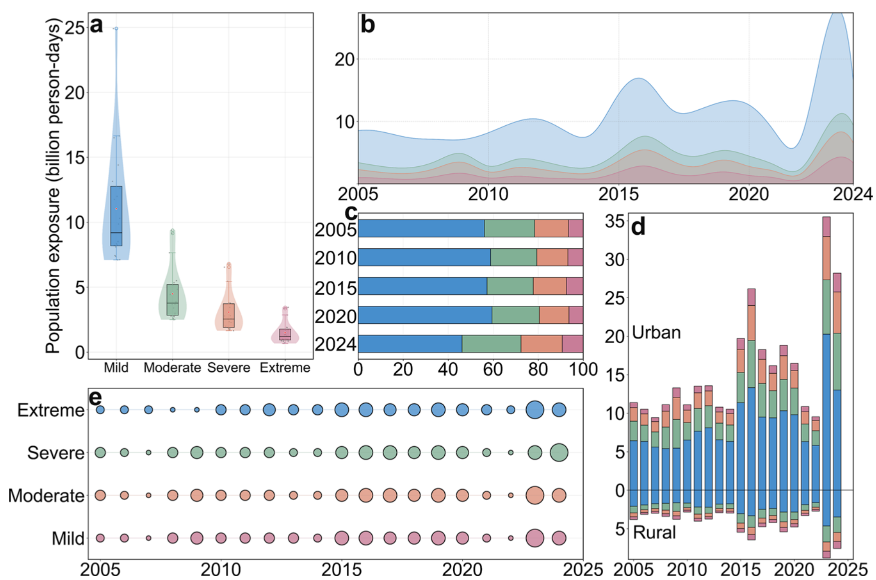


**Fig. 5 | Spatiotemporal patterns of population exposure to wet-bulb temperature across different intensity levels.** **a** Statistical distribution of population exposure across different levels; **b** interannual trends of population exposure by intensity levels (2005–2024); **c** proportional composition of exposure levels in representative years; **d** comparison of population exposure between urban and rural areas across different levels; **e** spatiotemporal evolution of urban–rural differences in population exposure. Units: billion person-days (**a**, **b**, **d**), percentage (**c**), billion person-days (**e**).

previous records. This indicates that recent humid-heat events are not only extreme in individual metrics but also remarkable in their accumulated thermal effects. The concurrent elevation of multiple parameters highlights a trend toward more compound and extreme humid-heat events.

We assess the hierarchical characteristics and spatiotemporal patterns of population exposure to humid heat, highlighting societal impacts. In terms of exposure intensity, mild exposure dominates considerably, exceeding other categories and exhibiting a distinct power-law distribution (Fig. 5a). This reflects the uneven nature of wet-bulb temperature (Tw) exposure: while most populations experience relatively low thermal stress, exposure to extreme heat remains limited. Time-series analysis indicates that exposure across all Tw levels was relatively stable from 2005 to 2018 but has risen noticeably in recent years, with mild and moderate categories increasing most markedly (Fig. 5b). Historically, mild exposure has consistently accounted for 70–80% of the total, yet its proportion is gradually declining, whereas moderate and higher exposure levels show sustained upward trends (Fig. 5c), pointing to an overall intensification. Urban–rural comparisons reveal marked spatial heterogeneity: urban areas exhibit higher exposure across all categories than rural areas, and this gap continues to widen over time (Fig. 5d). UHI effects are the primary driver of this disparity, and continued increases in urban population density further amplify exposure risks.

We evaluate hierarchical characteristics of population exposure and their spatiotemporal patterns to shed light on the impacts of humid heat events on human society. Regarding population exposure intensity classification, mild exposure demonstrates absolute predominance, with population exposure importantly exceeding other grades and manifesting distinct power-law distribution characteristics (Fig. 5a). This distribution pattern reflects the non-uniform nature of Tw exposure, whereby the majority of populations experience relatively low-intensity thermal stress, while populations subjected to extreme high-temperature exposure remain comparatively limited. Time series analyses reveal that exposure across all Tw grades remained relatively stable during 2005–2018, yet recent years have witnessed pronounced ascending trends, with mild and moderate exposure demonstrating the most conspicuous increases (Fig. 5b). From the perspective of historical evolution in proportional composition, mild exposure consistently maintains a dominant share of 70–80%, yet its proportion demonstrates gradual declining trajectories, while moderate and higher-grade exposure proportions exhibit sustained ascending trends (Fig. 5c), indicating overall upward shifts in exposure intensity. Urban–rural comparative analyses reveal pronounced spatial heterogeneity characteristics: exposure across all grades in urban areas substantially exceeds that in rural areas, with this disparity continuously expanding over time (Fig. 5d). The superimposed effects of UHI phenomena constitute the primary causative factor underlying this phenomenon, while sustained growth in urban population density further amplifies exposure risks.

More refined analyses of urban–rural differences reveal complex temporal fluctuations in exposure disparities across all gradations, with a pronounced amplification observed between 2019 and 2024 (Fig. 5e). This period aligns with accelerated urbanization and an increased frequency of extreme climate events, underscoring the growing challenges faced by urban areas in mitigating humid heat exposure risks.

## Discussion

In this study, we propose a UHI effect framework not previously reported and unravel that the urbanization's directional influence on Tw is not fixed but is substantially regulated by climatic background and geographical environmental conditions, showing complexity and spatial heterogeneity of urban climate effects. Our documented latitudinal gradient patterns are consistent with projections derived from the Clausius–Clapeyron relationship[39,40,56,57], while the concentrated high-value distributions observed at low latitudes align with prior global analyses of Tw[19,21,28]. This agreement reinforces the validity of both the data and the analytical framework employed. Building on this robust foundation, our long-term observational records reveal an important acceleration in the rise of global Tw after 2020, approximately five years earlier than the timing projected in the IPCC Sixth Assessment Report for the acceleration of global warming[12]. This finding delivers critical empirical evidence for climate change detection and attribution research. The physical mechanisms driving this earlier-than-expected acceleration can be attributed to a pronounced amplification in the exponential increase of sustainable water vapor content within the lower-to-middle troposphere in recent years, combined with a nonlinear enhancement of latent heat flux exchange processes at ocean–atmosphere interfaces[48,58,59]. These results imply that future humid-heat risks will intensify considerably, posing severe and remarkable challenges to global public health security and climate adaptation capacity. Urgent policy interventions and adaptive planning are required to mitigate escalating impacts on vulnerable populations and infrastructure.

Urban-scale comparative analysis reveals critical regulatory roles of urban development stages in shaping urban–rural temperature differences (Tw), bridging a key knowledge gap in previous studies that have insufficiently accounted for developmental differentiation in assessments of urbanization effects[24,59]. Emerging cities exhibit an importantly larger urban–rural Tw gradients than mature cities, alongside more pronounced interannual Tw variability. This divergence arises from the distinct restructuring of surface energy balance processes driven by differences in urbanization intensity and development rates. During accelerated urbanization, rapid land-cover transformation and concentrated infrastructure development fundamentally reshape spatial patterns of surface albedo, roughness, and evapotranspiration capacity[60,61], leading to marked shifts in sensible-to-latent heat flux ratios and substantially amplifying the magnitude of Tw responses[2,24,62–64].

Our newly developed "intensity-sensitivity coupling" theoretical framework reveals the fundamental physical mechanisms through which urbanization differentially affects Tw, overcoming theoretical limitations of earlier studies that relied on single-factor assumptions[65–67]. At the core of this framework is the representation of Tw as a nonlinear composite function of temperature and water vapor pressure, where the response intensity to urbanization-induced perturbations is governed by multiplicative effects between partial derivative sensitivity coefficients and the magnitude of environmental perturbations. Based on the first law of thermodynamics and vapor phase transition theory, the sensitivity coefficient of Tw to temperature, $\partial Tw/\partial T$, is largely influenced by the relationship between saturated water vapor pressure and temperature, as captured by the Clausius–Clapeyron equation[49]. The exponential increase of saturated water vapor pressure with temperature leads to a pronounced rise in temperature sensitivity under high-temperature conditions. In contrast, the sensitivity coefficient of Tw to water vapor pressure, $\partial Tw/\partial e$, is determined by the ratio of the psychrometric constant to local atmospheric pressure ($P$), which is itself modulated by local temperature and humidity conditions[68].

In low-latitude tropical oceanic and monsoon climates, vapor pressure sensitivity coefficients range from 0.8 to 1.0. This elevated sensitivity arises from the near-saturated atmospheric conditions prevalent in these regions, which cause the Tw to respond sharply to slight changes in vapor pressure[21,69,70]. Although urbanization-induced suppression of surface evapotranspiration remains relatively modest in such contexts, typically under 15%, the high vapor pressure sensitivity amplifies the resulting perturbations, leading to substantial negative contributions to Tw. Nevertheless, abundant moisture advection from oceans and active convective systems help sustain high background vapor pressures across tropical regions, thereby intrinsically limiting the development of UDI effects[36,71]. This constraint is reflected in the small absolute magnitude of urban–rural vapor pressure differences. In contrast, temperature perturbations caused by UHI effects via enhanced sensible heat fluxes exert more pronounced positive contributions to Tw. These are further amplified through the corresponding sensitivity coefficients, ultimately resulting in a systematic elevation of urban Tw compared to suburban values.

In mid-to-high latitude continental climate regions, marked seasonal aridity leads to comparatively balanced sensitivity coefficients for both temperature and water vapor pressure (each ranging between 0.4 and 0.6). Against this climatic backdrop, urbanization-driven expansions of impervious surfaces and pronounced reductions in vegetation cover strongly suppress surface evapotranspiration, resulting in decreased local atmospheric water vapor pressure[72]. The resulting perturbation in water vapor pressure propagates via moderate sensitivity coefficients, generating negative effects that numerically offset or exceed the positive contributions from UHI temperature increments transmitted through thermal sensitivity pathways. This leads to the emergence of reverse gradient patterns wherein urban Tw fall below those in suburban areas. Moreover, the naturally lower background humidity levels in mid-to-high latitudes provide greater scope for effective evapotranspiration regulation, further amplifying UDI effects. Notably, anthropogenic heat emissions, a major component of urbanization, also contribute directly to Tw patterns through enhanced sensible heat fluxes, an effect particularly evident within high-density urban cores[73,74]. This systematic analysis of multi-scale and multi-factor coupling mechanisms not only advances the scientific understanding of the physical processes underlying urban climate effects but also offers a critical theoretical foundation for accurately predicting and regulating urban humid heat environments across diverse climatic regimes.

Analysis of urban morphological characteristics reveals distinct regulatory mechanisms through which various elements influence $\Delta Tw$. Notably, vegetation coverage shows no important correlation with $\Delta Tw$ ($p > 0.05$), which may arise from the competing effects of evapotranspiration: cooling and humidification[36,41]. These counteracting processes likely neutralize the net impact of vegetation on urban–rural temperature differences. By clarifying the physical mechanisms by which urbanization drives divergent Tw responses under different climatic backgrounds, this study provides a mechanistic interpretation of recently observed regional Tw variations[2,75] and lays the groundwork for a deeper understanding of compound effects in urban humid heat environments[36,38]. Future research should focus on exploring the evolution of coupling mechanisms across multiple timescales to improve understanding of seasonal and interannual regulatory processes affecting sensitivity distributions. Such insights will offer precise scientific support for developing tailored urban climate adaptation strategies.

Our comprehensive population exposure risk assessment system advances beyond the theoretical constraints of prior evaluations based solely on air temperature, thereby addressing a critical scientific shortcoming in conventional research that underestimates compound humid heat risks[76,77]. By quantifying the impacts of humid heat events on global populations across multiple dimensions, we uncover three central patterns in the evolution of humid heat exposure risk: first, exposure distributions follow power-law patterns dominated by mild-risk events, aligning closely with theoretical predictions of global population exposure[19]. This reflects the long-tail characteristics of humid heat stress, wherein a majority of the population experiences moderate but persistent pressure. Second, all grades of exposure exhibit important upward trends over time, with sustained growth in the proportion of populations facing moderate-to-severe exposure, indicating a systematic intensification of global humid heat risks. Third, urban populations consistently experience higher exposure levels than rural ones, with a progressively widening gap, quantitatively affirming the role of urbanization in amplifying health risks[14].

Characterization of extreme humid heat events reveals critical signals of climate system transitions. During 2023–2024, cumulative heat index events exceeding 30 °C days not only set historical records but also indicated that compound humid heat events have entered remarkable intensity regimes. An intensified temporal clustering of high-grade humid heat episodes reflects increasing heterogeneity in atmospheric energy distribution. Alarmingly, the intensity of recent extreme humid heat events approaches levels projected for the mid-21st century[69], suggesting that dangerous humid heat conditions are emerging decades ahead of climate model predictions, a sign of accelerated climate system responses. Under RCP8.5 scenarios, the global population exposed to hazardous Tw is projected to reach 750 million[78]. When combined with the superimposed effects of urbanization[79], humid heat stress, identified as the dominant environmental stressor among multiple forms of human thermal exposure[36,80,81], poses a fundamental threat to human habitability[3,82]. These findings underscore the urgent need for science-based strategies to mitigate and manage urban humid heat risks.

This study extends beyond traditional UHI frameworks by clarifying the distinct mechanisms through which urbanization influences humid heat conditions in human settlements. The findings provide a theoretical basis for risk assessments based on climate sensitivity and for the design of targeted urban adaptation strategies. These results have important implications for sustaining climate resilience in global urban systems and for supporting long-term human survival and development. While ERA5 has inherent limitations in spatial resolution (~31 km) and urban process representation, our comprehensive validation against ground observations across all 56 cities ($R^2 = 0.97$) confirms its reliability for analyzing regional climatic influences on urban-scale humid heat patterns. Future advances in higher-resolution climate datasets would further enhance our understanding of fine-scale urban thermal heterogeneity and support more precise adaptation strategies.

Future research should test the applicability of the proposed mechanisms in vulnerable regions and improve the accuracy of compound climate risk predictions. As global humid heat risks continue to intensify, urban planners and emergency management agencies must develop region-specific regulatory strategies that account for spatial differences in climate sensitivity, with particular emphasis on enhancing climate resilience in rapidly urbanizing areas.

## Materials and methods

### City selection

A globally representative urban sample was selected based on the United Nations World Urbanization Prospects 2018 dataset through multi-dimensional screening criteria[1]. The selection criteria encompassed: (1) population scale, prioritizing megacities with projected populations exceeding 10 million by 2035 to ensure global significance; (2) geographical representativeness, ensuring comprehensive coverage across latitudinal zones (tropical, subtropical, temperate, and polar regions) and balanced representation of coastal and inland locations; and (3) climatic diversity, guaranteeing inclusion of all 13 secondary classifications within the Köppen climate classification system. Through this systematic multi-dimensional screening approach, 56 cities were ultimately selected as study subjects. Detailed information regarding geographical coordinates, population size, climate types, and other relevant characteristics is provided in Supplementary Table 1. This urban sample demonstrates robust global representativeness, providing a solid foundation for the generalizability and scientific validity of the research findings.

### Data collection and preprocessing

Meteorological data comprised wet-bulb temperature calculations primarily derived from the ERA5 reanalysis dataset, validated against the Global Station Daily Maximum Wet-bulb Temperature dataset (GSDM-WBT), which encompasses homogenized records from 1834 meteorological stations globally spanning 1981–2020, with mean biases of −0.48 and 0.34 °C relative to other datasets following climatol quality control procedures[83]; land surface temperature data were obtained from the MODIS/Terra land surface temperature daily product (MOD11A1 Version 6.1), providing global coverage at 1-km spatial resolution; atmospheric variables, including 2-meter dewpoint temperature, surface pressure, and relative humidity, were sourced from the ERA5 reanalysis dataset[84], which provides high spatiotemporal resolution global meteorological fields from 1940 to present. Population data were primarily derived from the GlobPOP global population distribution dataset[85], which employs a data fusion framework to provide continuous gridded population density at 30-arcsecond spatial resolution, supplemented by the LandScan dataset[86] that utilizes remote sensing technologies and machine learning algorithms to characterize ambient population distribution patterns, with missing temporal data interpolated using published literature sources[87]. Ancillary datasets included standardized geographic data products from Natural Earth for urban boundary delineation, the PKU GIMMS NDVI product from Peking University for vegetation indices[88], and the Annual VIIRS Nighttime Light product Version 2 provided by the Earth Observation Group[89]. All datasets represent publicly available products, ensuring research reproducibility, and underwent spatial resampling to uniform resolution, temporal synchronization, and comprehensive quality control procedures to maintain analytical consistency and reliability.

### Calculation of wet-bulb temperature

Following established methodologies from previous studies[24,90,91] and implementing the algorithm described by Davies-Jones[92], we calculated global wet-bulb temperatures (Tw) for 1980–2023. The computation employed an iterative solution method based on thermodynamic principles and fundamental psychrometric relationships, which circumvents computational biases identified in existing open-source code repositories. To ensure computational accuracy and convergence efficiency, the iteration accuracy threshold is set to 0.01 °C with a maximum of 100 iterations. In practice, the algorithm typically converges to a solution meeting the accuracy requirements within 10 iterations under most meteorological conditions. This numerical iteration method demonstrates high computational stability and broad applicability, effectively handling wet-bulb temperature calculations across various meteorological conditions. The calculated actual water vapor pressure ($e_a$) data will also be utilized in subsequent analyses of wet-bulb temperature response mechanisms.

Additionally, we conducted physical plausibility checks on all computational results to ensure the wet-bulb temperature does not exceed the dry-bulb temperature and complies with thermodynamic constraints. The reliability of our calculations was validated through comparative analysis of cumulative distribution functions between calculated values and the global station observational dataset[83]. This validation method was selected for its robust capability in detecting monotonic trends in time series data.

### Reliability assessment of wet-bulb temperature

To quantify the uncertainty associated with wet-bulb temperature (Tw) calculated from ERA5 data, we compiled daily surface observations (air temperature, relative humidity, and pressure) for 56 cities during 2005–2024. These data were sourced from the Global Summary of the Day (GSOD) dataset[93], provided by the National Centers for Environmental Information (NCEI) under the National Oceanic and Atmospheric Administration. The GSOD dataset boasts extensive global station coverage (Supplementary Fig. 11) and is widely recognized in the academic community for its rigorous quality control and long-term records. For this study, we selected station data corresponding to our 56 study cities from the GSOD dataset, with these stations covering diverse geographical and climatic backgrounds, providing a solid and reliable observational benchmark for subsequent validation analyses. Using the same algorithm applied to ERA5, these observations were converted to station-based Tw (hereafter Tw_obs). Hourly pairs of ERA5-derived Tw (Tw_ERA5) and Tw_obs were time-matched. The comparison produces five key findings.

### High overall agreement

The aggregated hexbin scatterplot exhibits a coefficient of determination of $R^2 = 0.97$ and a linear regression slope close to 1.00 between Tw_ERA5 and Tw_obs (Supplementary Fig. 12a). This indicates that ERA5 faithfully reproduces large-scale wet-heat signals and shows high consistency with ground observations.

### Controlled absolute error

Statistical analysis of all samples reveals that 65.3% of absolute biases $|\text{Tw\_ERA5} - \text{Tw\_obs}|$ are ≤ 2 °C, with 89.7% controlled within 5 °C (Supplementary Fig. 12b). This confirms that ERA5 data provide reliable wet-bulb temperature estimates in the vast majority of cases.

### No systematic spatial bias

Analysis of the multi-year mean bias spatial distribution for 2005–2024 shows that mean biases for individual cities range from −1.2 to 1.5 °C, with no discernible latitudinal or longitudinal gradients or concentrated systematic bias regions (Supplementary Fig. 12c). This suggests that the ERA5 data's performance in calculating Tw remains relatively consistent across different geographical regions.

### Limited coastal–inland contrast

Further comparison of bias distributions for coastal and inland cities reveals nearly identical violin plot shapes, with medians close to 0 °C and an interquartile range difference of less than 0.4 °C (Supplementary Fig. 12d). This indicates robust performance of ERA5 data in calculating Tw across different geographical types.

### Temporal stability

Monthly and annual boxplots of bias (Supplementary Fig. 13) demonstrate median bias fluctuations confined to within ±0.3 °C, with no apparent decadal drift or systematic changes over the two-decade time series. This indicates good temporal stability in the performance of ERA5 data.

In summary, based on the GSOD validation results and through independent and detailed station-level comparative validations performed for each of the cities in this study (e.g., Supplementary Figs. 14–31), ERA5 data exhibits small errors, good spatial consistency, and temporal stability in Tw calculation. While we acknowledge that specific statistical metrics (e.g., $R^2$) might vary slightly across different cities due to unique micro-climatic environments and station representativeness within a large grid cell, overall, the validation results for the vast majority of cities are highly consistent with our aggregated findings, effectively meeting the accuracy requirements for regional-scale urban wet-heat environment analyses conducted in this study.

### Urban–rural spatial classification and wet-bulb temperature differential analysis

Based on the obtained wet-bulb temperature data, we employs nighttime light data for urban–rural spatial classification and temperature differential analysis. Initially, the RBI is calculated to standardize nighttime light data[94,95] using the formula:

$$\mathrm{RBI} = \frac{L_{\mathrm{i}} - L_{\min}}{L_{\max} - L_{\min}} \tag{1}$$

where $L_{\mathrm{i}}$ represents the nighttime light brightness value for pixel $i$, while $L_{\min}$ and $L_{\max}$ denote the minimum and maximum values within the study domain, respectively. This standardization process eliminates dimensional effects, making brightness values comparable across different regions. It is important to note that $L_{\min}$ and $L_{\max}$ are determined within each city's administrative boundary independently, ensuring that the RBI reflects the relative spatial structure within each city rather than absolute brightness levels across different cities.

The K-means clustering algorithm is applied to standardized RBI values for five-level spatial classification, with this unsupervised machine learning approach automatically identifying intrinsic spatial structures within nighttime light data while avoiding subjective biases inherent in traditional threshold-setting methods. The clustering process sets $k = 5$ clusters, employs Euclidean distance as the similarity measure, and iteratively optimizes to minimize intra-cluster variance. Algorithm convergence criteria are established with consecutive iterations requiring centroid movement distances less than 0.001, ensuring mathematical rigor in classification results. After algorithm convergence, cluster centers are ranked by magnitude and labeled sequentially as high-density urban core, medium-density urban built-up, low-density urban expansion, peri-urban transition zone, and rural natural area. By ranking clusters according to their mean RBI values rather than using arbitrary labels, this method effectively eliminates the influence of algorithm initialization randomness on outcomes and ensures consistent interpretation across all cities. Importantly, this classification is data-driven and objective, avoiding subjective threshold-setting that could introduce researcher bias. The five-level classification is reorganized into a binary urban–rural classification system, avoiding the subjective limitations of the traditional site classification method. Urban Areas comprise the first three categories (high-density urban core, medium-density urban built-up, low-density urban expansion), while Rural Areas include the latter two categories (peri-urban transition zone, rural natural area). Based on this binary classification, area-weighted average wet-bulb temperatures are calculated separately for urban and rural regions. The urban–rural wet-bulb temperature differential is computed using:

$$\Delta Tw(i,t) = Tw(Urban) - Tw(Rural) \tag{2}$$

where Tw(Urban) and Tw(Rural) represent average wet-bulb temperatures for urban and rural regions at time $t$, respectively.

Cities within the study region are classified based on urban area proportion (UAP), defined as the ratio of urban areas (sum of high-density urban core, medium-density urban built-up, and low-density urban expansion areas) to the total administrative area. Cities are categorized in descending order of UAP as: urbanized cities (UAPå 50%), transitional cities (UAP = 40–50%), compact cities (UAP = 30–40%), rural cities (UAP = 20–30%), and emerging cities (UAP < 20%).

It is crucial to emphasize that this classification reflects urban spatial form compactness rather than economic development level or urbanization quality. The category labels describe the spatial configuration of built-up areas within administrative boundaries, not the city's development stage. For instance, Tokyo (UAP = 18.3%) and Osaka (UAP = 17.6%) are classified as emerging cities because their administrative boundaries (Tokyo Prefecture and Osaka Prefecture) encompass extensive mountains (e.g., western Tama mountains in Tokyo, eastern Ikoma mountains in Osaka), forest reserves, and agricultural land, with actual high-, medium-, and low-density built-up areas occupying less than 10% of total administrative area. This "compact core + vast hinterland" spatial morphology does not imply these cities are economically "underdeveloped"; rather, it reflects Japanese prefectural administrative divisions where administrative boundaries far exceed actual built-up areas, and preservation of extensive natural spaces within city limits. Similarly, Seoul (UAP = 22.4%) is classified as a Rural City due to extensive mountains (Bukhansan National Park, Gwanaksan) and Han River greenbelts within Seoul special city boundaries, occupying approximately 40% of the total area.

It is important to note that UAP is a cross-sectional spatial indicator that captures the current spatial configuration of urban built-up areas, not a longitudinal temporal indicator reflecting urban growth trajectories. While cities with low UAP (e.g., Tokyo) may have experienced rapid growth in earlier periods, their current spatial morphology—characterized by compact cores and extensive hinterlands—determines their present-day wet-bulb temperature patterns.

This spatial morphology classification has direct physical significance for wet-bulb temperature analysis. Cities with high UAP values (e.g., Kinshasa, UAP = 52.1%, urbanized city) exhibit continuous sprawling built-up areas where extensive impervious surfaces generate intense sensible heat release, resulting in strong urban–rural wet-bulb temperature gradients. Conversely, cities with low UAP values (e.g., Tokyo, emerging city) feature compact urban cores surrounded by extensive vegetation-covered areas that provide substantial evapotranspiration cooling effects, thereby mitigating wet-bulb temperature gradients despite potentially high UHI intensity in core areas. Preliminary validation shows that Urbanized Cities exhibit importantly higher average urban–rural Tw gradients (mean ΔTw = 1.8 ± 0.6 °C) compared to emerging cities (mean ΔTw = 0.7 ± 0.3 °C), confirming that UAP is an effective predictor of wet-bulb temperature spatial patterns.

Area statistics for each city are computed through raster data spatial statistical analysis, employing pixel counting methodology to ensure area calculation precision. All spatial analysis processes employ identical geographic coordinate systems (WGS 84) and projection methods (equal-area projection) to maintain spatial data processing consistency and enable direct cross-city comparisons.

### Wet-bulb temperature difference driving mechanism elucidation and urban characteristic factor identification methodology

We employed a physically grounded attribution framework to decompose urban–rural wet-bulb temperature differences (ΔTw) into contributions from temperature and water vapor pressure changes, thereby elucidating the formation mechanisms of urban–rural Tw difference spatial patterns. This approach is based on partial derivative sensitivity analysis derived from the psychrometric wet-bulb temperature equation, which achieves quantitative separation of the independent effects of heat island and dry island phenomena by constructing partial differential equation systems.

The urban–rural Tw difference was approximated using first-order Taylor expansion as:

$$\Delta \mathrm{Tw} \approx (\partial Tw/\partial T) \times \Delta T + (\partial Tw/\partial e) \times \Delta e \tag{3}$$

where $\Delta T$ and $\Delta e$ represent urban–rural differences in air temperature and water vapor pressure, respectively. The partial derivatives $\partial \mathrm{Tw}/\partial T$ and $\partial \mathrm{Tw}/\partial e$ are sensitivity coefficients quantifying how Tw responds to unit changes in each variable. Global sensitivity analysis was conducted using the Sobol method to quantify the wet-bulb temperature's sensitivity to different meteorological parameters, utilizing 128 Sobol sequences for parameter sampling and calculating first-order sensitivity indices (Si) and total effect indices (STi). These sensitivity coefficients were calculated analytically from the psychrometric equation using local meteorological conditions (temperature, vapor pressure, and atmospheric pressure) at monthly time steps.

This physically derived approach avoids multicollinearity issues inherent in statistical regression, as the attribution is mechanistically grounded in thermodynamic first principles rather than correlations. Temporal analyses were conducted at monthly, seasonal, and annual scales. Pearson correlation analysis and ordinary least squares regression modeling were employed to quantify statistical relationships between absolute urban–rural wet-bulb temperature differences and sensitivity indices. Study regions were categorized into urban warming groups ($\Delta \mathrm{Tw} > 0$) and urban cooling groups ($\Delta \mathrm{Tw} \leq 0$) for comparative analysis. To validate the linear approximation, we performed diagnostic checks, including normality tests (Shapiro–Wilk test, $p > 0.05$) on residuals (observed minus attributed ΔTw), confirming the adequacy of the first-order Taylor expansion for capturing dominant attribution effects. Statistical inference validity was further verified through spatial autocorrelation testing and independent samples t-tests.

We selected four urban characteristic variables: population density, vegetation coverage (NDVI), urban area, and shape index (SHAPE) to analyze their effects on urban–rural wet-bulb temperature differences (ΔTw), representing anthropogenic activity intensity, ecosystem regulation functions, urbanization scale effects, and boundary geometric characteristics[54], respectively. Shape index was calculated using the formula:

$$SHAPE = (0.25 \times perimeter) / \sqrt{area} \tag{4}$$

Statistical analysis comprised two main components: regression analysis and cluster analysis. Regression analysis employed polynomial fitting methods to establish nonlinear relationship models between urban characteristic variables and wet-bulb temperature differences, with parameters estimated using the least squares method, model performance evaluated through the coefficient of determination and Pearson correlation coefficients, and statistical inference conducted at predetermined significance levels. Cluster analysis utilized the K-means unsupervised learning algorithm to identify urban typological grouping patterns, with data pre-standardized, optimal cluster numbers determined through the elbow method and silhouette coefficient, and confidence ellipses drawn for each cluster to characterize distribution features.

It is crucial to note that the city classifications (e.g., "emerging cities" and "urbanized cities") in this study are defined based on the dynamics of night-time light index data, specifically the rate and pattern of change observed during the study period (2005–2024), rather than their absolute economic development level or static urbanization status. Specifically, "emerging cities" and "urbanized cities" emphasize cities that experienced important land-cover transformation, concentrated infrastructure development, or rapid population influx/expansion processes during the study period. Consequently, some highly developed and extensively urbanized cities, such as Tokyo and Osaka, might not be categorized as "urbanized cities" (which denotes rapid change) if their rate of change during the study period was relatively low, or if their vast urban extent and well-developed green infrastructure (e.g., parks) influenced the percentage contribution of the night-time light index. Instead, they might be classified as "emerging cities" or even "rural cities" based on their dynamic characteristics. This classification approach aims to capture the dynamic development trajectories of cities during the study period and their impact on surface energy balance processes, consistent with previous studies that accounted for developmental differentiation in assessing urbanization effects.

Temperature change intensity-trend relationships are analyzed using multi-temporal scale quantitative methods. Data preprocessing includes NaN value removal and valid observation thresholds, with regional classification into Southern and Northern Hemispheres for accurate seasonal analysis windows. Intensity indicators are calculated through multi-year averages, while trend parameters are determined via linear regression of interannual sequences and converted to decadal change rates. Analytical approaches encompass annual means, seasonal analyses (summer and winter), and multi-window moving averages (3-, 5-, and 7-year) to comprehensively capture intensity-trend characteristics across temporal scales. This approach helps to effectively filter out high-frequency noise, thereby revealing more clearly the oscillatory characteristics and underlying trends of ΔTw intensity over longer timescales. Statistical analysis employs Pearson correlation coefficients to quantify linear relationship strength, with significance assessed through two-tailed t-tests ($\alpha = 0.05$). Four-quadrant analysis using intensity median and zero-trend boundaries quantifies spatial distribution characteristics of different combination patterns, providing statistical evidence for understanding urban thermal environment evolutionary dynamics.

### Humid heat event identification and characterization

We employed a percentile-based threshold approach to identify and characterize humid heat events using daily maximum wet-bulb temperature (Tw) data spanning the period from 2005 to 2024. Thresholds were established using the full-period percentile method, whereby percentiles were calculated from the entire 20-year climatological baseline to ensure temporal consistency and avoid artificial trends that may arise from moving baseline periods. This approach provides a stationary reference frame that enables robust detection of humid heat events across the study period while maintaining comparability between different years and regions.

Humid heat events were defined as continuous periods during which the daily maximum wet-bulb temperature exceeded the 75th percentile threshold for at least one consecutive day. To comprehensively capture the intensity spectrum of humid heat exposure, we established a four-tier classification system based on wet-bulb temperature percentiles derived from the complete study period: (a) mild humid heat events (MHH, $P75 \le Tw < P90$); (b) moderate humid heat events (MOH, $P90 \le Tw < P95$); (c) severe humid heat events (SEH, $P95 \le Tw < P99$); and (d) extreme humid heat events (EXH, $Tw \ge P99$). All percentile thresholds were calculated independently for each grid cell to account for local climatological variations while maintaining consistent relative intensity definitions across the study domain. To ensure the robustness and comparability of humid heat event classification thresholds, this study utilized the complete 20-year dataset from 2005 to 2024 as the climatological baseline for calculating daily percentile thresholds for each city. This fixed-baseline approach effectively avoids artificial trends that might be introduced by using a moving baseline, thus ensuring the stability of thresholds and the reliability of event detection.

It is crucial to emphasize that this study employs a percentile-based threshold method rather than fixed absolute temperature values. This approach allows the humid heat event thresholds to dynamically vary with geographical location (climate and latitude of different cities) and season (different days of the year). This ensures a fair and meaningful comparison of humid heat events across diverse climatic backgrounds and accurately captures local specific humid heat characteristics.

For each identified humid heat event, we calculated seven key metrics to comprehensively characterize event properties and population exposure. Frequency ($F$) was quantified as the annual count of humid heat days exceeding the respective threshold, expressed in days per year. Duration characteristics were captured through mean duration, calculated as the average duration of all humid heat events within a year, and maximum duration, representing the longest event duration in each year. Intensity metrics included mean intensity, defined as the average daily excess wet-bulb temperature during humid heat events relative to the threshold, and maximum intensity, representing the highest daily excess wet-bulb temperature across all events within a year.

The cumulative heat index (CHI) was computed as the sum of daily excess wet-bulb temperatures across all humid heat days, mathematically expressed as:

$$CHI = \sum_{i=1}^{n} \sum_{j=1}^{D_i} \left( T_{w,ij} - T_{threshold} \right) \tag{5}$$

where $T_{\mathrm{w,ij}}$ represents the wet-bulb temperature on day $j$ of event $i$, $T_{\mathrm{threshold}}$ is the respective percentile threshold, $D_{\mathrm{i}}$ is the duration of event $i$, and $n$ is the total number of events per year. This metric provides a comprehensive measure of total heat accumulation throughout each year, integrating both the intensity and duration components of humid heat exposure. Population exposure ($E$) was calculated to quantify the total person-days of humid heat exposure experienced by the population in each location, following the equation:

$$E = P \times F \tag{6}$$

where $P$ represents the grid cell population, and $F$ denotes the humid heat frequency, defined as the annual count of days when wet-bulb temperature exceeds the respective percentile threshold. Regional synthesis was achieved through spatial aggregation methods tailored to each metric type. Frequency and population exposure were calculated by summing values across all grid cells within each study region, reflecting the cumulative nature of these exposure measures. Intensity metrics were computed using area-weighted averaging to provide representative regional characteristics while preserving spatial variability information.

## Data availability

ERA5 reanalysis dataset for atmospheric variables was obtained from https://cds.climate.copernicus.eu/datasets/reanalysis-era5-pressure-levels-monthly-means?tab=overview. The MODIS/Terra Land Surface Temperature daily product (MOD11A1 Version 6.1) was accessed from https://ladsweb.modaps.eosdis.nasa.gov/search/order/1. The Global Station Daily Maximum Wet-bulb Temperature dataset (GSDM-WBT) is available through https://zenodo.org/records/7014332. The GlobPOP global population distribution dataset was downloaded from https://zenodo.org/records/11179644. The LandScan global population dataset is available at https://landscan.ornl.gov/. Standardized geographic data products from Natural Earth were accessed through https://www.naturalearthdata.com/. The PKU GIMMS NDVI product from Peking University was obtained from https://zenodo.org/records/8253971. The Annual VIIRS Nighttime Light product Version 2 from the Earth Observation Group (EOG) is available at https://eogdata.mines.edu/products/vnl/#v1. All datasets represent publicly available products that ensure research reproducibility. The global daily meteorological data used in this study are from the Global Summary of the Day (GSOD) dataset released by the NOAA National Centers for Environmental Information (NCEI), which is available at the official archive website: https://www.ncei.noaa.gov/data/global-summary-of-the-day/archive/. Data sharing not applicable to this article as no datasets were generated or analyzed during the current study.

## Code availability

The data in this study were analyzed, and the figures were created using Python. All relevant codes used in this work are available from the corresponding author upon reasonable request.

Received: 2 October 2025; Accepted: 12 March 2026;
Published online: 26 March 2026

## References

1. United Nations, Department of Economic and Social Affairs, Population Division. World Urbanization Prospects: The 2018 Revision (United Nations, 2019). https://population.un.org/wup/assets/WUP2018-Report.pdf.
2. Zhang, K. et al. Increased heat risk in wet climate induced by urban humid heat. *Nature* **617**, 738–742 (2023).
3. Pal, J. S. & Eltahir, E. A. B. Future temperature in Southwest Asia projected to exceed a threshold for human adaptability. *Nat. Clim. Change* **6**, 197–200 (2015).
4. Chan, D., Gebbie, G. & Huybers, P. An improved ensemble of land surface air temperatures since 1880 using revised pair-wise homogenization algorithms accounting for autocorrelation. *J. Clim.* **37**, 2325–2345 (2024).
5. Liao, W., Wang, L., Liu, X., Chan, D. & Li, D. Standardized heat islands and persistence drive modeled urban heat events. *Nat. Cities* **2**, 857–864 (2025).

6. Lin, X., Wang, Y. J. & Song, L. C. Urbanization amplified compound hot extremes over the three major urban agglomerations in China. *Geophys. Res. Lett.* **51**, e2023GL106644 (2024).
7. Sun, Y., Zhang, X. B., Ren, G. Y., Zwiers, F. W. & Hu, T. Contribution of urbanization to warming in China. *Nat. Clim. Change* **6**, 706(2016).
8. Chakraborty, T. C. & Qian, Y. Urbanization exacerbates continental- to regional-scale warming. *One Earth* **7**, 1387–1401 (2024).
9. Robine, J.-M. et al. Death toll exceeded 70,000 in Europe during the summer of 2003. *C. R. Biol.* **331**, 171–U178 (2008).
10. Yang, J. et al. Projecting heat-related excess mortality under climate change scenarios in China. *Nat. Commun.* **12**, 1039 (2021).
11. García-León, D. et al. Current and projected regional economic impacts of heatwaves in Europe. *Nat. Commun.* **12**, 5807 (2021).
12. IPCC. *Climate Change 2023: Synthesis Report* (Cambridge University Press, 2023).
13. Wang, S. S. et al. Dual impact of global urban overheating on mortality. *Nat. Clim. Change* **15**, 497 (2025).
14. Tuholske, C. et al. Global urban population exposure to extreme heat. *Proc. Natl. Acad. Sci. USA* **118**, e2024792118 (2021).
15. Zhang, L., Liao, W., Chen, X., Cheng, S. & Yang, J. Temporally compound heatwave and its interaction with urban heat island over mainland China. *Earth's Future* **13**, e2025EF006490 (2025).
16. Perkins-Kirkpatrick, S. E. & Lewis, S. C. Increasing trends in regional heatwaves. *Nat. Commun.* **11**, 3357 (2020).
17. Trancoso, R. et al. Heatwaves intensification in Australia: a consistent trajectory across past, present and future. *Sci. Total Environ.* **742**, 140521 (2020).
18. Wei, J. et al. Projecting the changes in multifaceted characteristics of heatwave events across China. *Earth's Future* **11**, e2022EF003387 (2023).
19. Raymond, C., Matthews, T. & Horton, R. M. The emergence of heat and humidity too severe for human tolerance. *Sci. Adv.* **6**, eaaw1838 (2020).
20. Budd, G. M. Wet-bulb globe temperature (WBGT)-its history and its limitations. *J. Sci. Med. Sport* **11**, 20–32 (2008).
21. Sherwood, S. C. & Huber, M. An adaptability limit to climate change due to heat stress. *Proc. Natl. Acad. Sci. USA* **107**, 9552–9555 (2010).
22. International Organization for Standardization. ISO 7243:2017 Ergonomics of the Thermal Environment — Assessment of Heat Stress Using the WBGT (Wet Bulb Globe Temperature) Index (ISO, 2017).
23. Li, C., Zhang, X. B., Zwiers, F., Fang, Y. Y. & Michalak, A. M. Recent very hot summers in Northern Hemispheric Land areas measured by wet bulb globe temperature will be the norm within 20 years. *Earth's Future* **5**, 1203–1216 (2017).
24. Wang, P., Leung, L. R., Lu, J., Song, F. & Tang, J. Extreme wet-bulb temperatures in China: the significant role of moisture. *J. Geophys. Res. Atmos.* **124**, 11944–11960 (2019).
25. Im, E.-S., Pal, J. S. & Eltahir, E. A. B. Deadly heat waves projected in the densely populated agricultural regions of South Asia. *Sci. Adv.* **3**, e1603322 (2017).
26. Ullah, I. et al. Projected changes in socioeconomic exposure to heatwaves in South Asia under changing climate. *Earth's Future* **10**, e2021EF002240 (2022).
27. Wang, F., Gao, M., Liu, C., Zhao, R. & McElroy, M. B. Uniformly elevated future heat stress in China driven by spatially heterogeneous water vapor changes. *Nat. Commun*. **15**, 4522 (2024).
28. Zhang, J., You, Q., Ren, G. & Ullah, S. Substantial increase in human-perceived heatwaves in eastern China in a warmer future. *Atmos. Res.* **283**, 106554 (2023).
29. Kalnay, E. & Cai, M. Impact of urbanization and land-use change on climate. *Nature* **423**, 528–531 (2003).
30. Sun, Y., Zhang, X., Ren, G., Zwiers, F. W. & Hu, T. Contribution of urbanization to warming in China. *Nat. Clim. Change* **6**, 706 (2016).
31. Yang, X. et al. Contribution of urbanization to the increase of extreme heat events in an urban agglomeration in East China. *Geophys. Res. Lett.* **44**, 6940–6950 (2017).
32. Koster, R. D. et al. Regions of strong coupling between soil moisture and precipitation. *Science* **305**, 1138–1140 (2004).
33. Sandholt, I., Rasmussen, K. & Andersen, J. A simple interpretation of the surface temperature/vegetation index space for assessment of surface moisture status. *Remote Sens. Environ.* **79**, 213–224 (2002).
34. Savenije, H. H. G. New definitions for moisture recycling and the relationship with land-use changes in the Sahel. *J. Hydrol.* **167**, 57–78 (1995).
35. Hao, L. et al. Urbanization alters atmospheric dryness through land evapotranspiration. *NPJ Clim. Atmos. Sci.* **6**, 149 (2023).
36. Chen, B., Kong, F., Meadows, M. E. & Yin, H. Wet-hot days increased faster than dry-hot days during the warm season in Chinese cities over the past four decades. *Commun. Earth Environ.* **6**, 582 (2025).
37. Moazzam, M. F. U. & Lee, B. G. Urbanization influenced SUHI of 41 megacities of the world using big geospatial data assisted with Google Earth Engine. *Sustain. Cities Soc*. **101**, 105095 (2024).
38. Luo, S. et al. Anthropogenic climate change and urbanization exacerbate risk of hybrid heat extremes in China. *J. Geophys. Res. Atmos.* **129**, e2024JD041568 (2024).
39. Willett, K. M., Gillett, N. P., Jones, P. D. & Thorne, P. W. Attribution of observed surface humidity changes to human influence. *Nature* **449**, 710–U716 (2007).
40. Trenberth, K. E., Dai, A., Rasmussen, R. M. & Parsons, D. B. The changing character of precipitation. *Bull. Am. Meteorol. Soc.* **84**, 1205–1217 (2003).
41. Yang, Y. et al. Regulation of humid heat by urban green space across a climate wetness gradient. *Nat. Cities* **1**, 871–879 (2024).
42. Shen, P. K., Zhao, S. Q. & Ma, Y. J. Perturbation of urbanization to Earth's surface energy balance. *J. Geophys. Res. Atmos.* **126**, e2020JD033521 (2021).
43. Zhao, L., Lee, X., Smith, R. B. & Oleson, K. Strong contributions of local background climate to urban heat islands. *Nature* **511**, 216–219 (2014).
44. Gimeno, L. et al. Major mechanisms of atmospheric moisture transport and their role in extreme precipitation events. *Annu. Rev. Environ. Resour.* **41**, 117–141 (2016).
45. Hou, Z. Y. et al. Radiative forcing reduced by early twenty-first century increase in land albedo. *Nature* **641**, 1162–1171 (2025).
46. Dematteis, G. et al. Interacting internal waves explain global patterns of interior ocean mixing. *Nat. Commun.* **15**, 7468 (2024).
47. Liu, Q., Dong, Q., Zhang, L. & Sun, C. Summer cooling island effects of blue-green spaces in severe cold regions: a case study of Harbin, China. *Build. Environ.* **257**, 111539 (2024).
48. Liao, W., Wang, L. & Liu, X. Standardized heat islands and persistence drive modeled urban heat events. *Nat. Cities* **2**, 857–864 (2025).
49. Da Silva, N. A. & Haerter, J. O. Super-Clausius-Clapeyron scaling of extreme precipitation explained by shift from stratiform to convective rain type. *Nat. Geosci.* **18**, 382–388 (2025).
50. Yang, J. et al. Local climate zone ventilation and urban land surface temperatures: Towards a performance-based and wind-sensitive planning proposal in megacities. *Sustain. Cities Soc.* **47**, 101487 (2019).
51. McGrane, S. J. Impacts of urbanisation on hydrological and water quality dynamics, and urban water management: a review. *Hydrol. Sci. J.* **61**, 2295–2311 (2016).
52. Chen, M. X., Zhou, Y., Hu, M. G. & Zhou, Y. L. Influence of urban scale and urban expansion on the urban heat island effect in metropolitan areas: case study of Beijing-Tianjin-Hebei urban agglomeration. *Remote Sens.* **12**, 3491 (2020).
53. Zhou, B., Rybski, D. & Kropp, J. P. The role of city size and urban form in the surface urban heat island. *Sci. Rep.* **7**, 4791 (2017).

54. Wang, C. L., Liu, Z. H., Du, H. L. & Zhan, W. F. Regulation of urban morphology on thermal environment across global cities. *Sustain. Cities Soc.* **97**, 104749 (2023).
55. Hao, M., Liu, X. & Li, X. Quantifying heat-related risks from urban heat island effects: a global urban expansion perspective. *Int. J. Appl. Earth Observ. Geoinf.* **136**, 104344 (2025).
56. Byrne, M. P. & O'Gorman, P. A. Understanding decreases in land relative humidity with global warming: conceptual model and GCM simulations. *J. Clim.* **29**, 9045–9061 (2016).
57. Sippel, S., Meinshausen, N., Fischer, E. M., Székely, E. & Knutti, R. Climate change now detectable from any single day of weather at global scale. *Nat. Clim. Change* **10**, 35 (2020).
58. Zhang, Y., Held, I. & Fueglistaler, S. Projections of tropical heat stress constrained by atmospheric dynamics. *Nat. Geosci.* **14**, 133 (2021).
59. Newth, D. & Gunasekera, D. Projected changes in wet-bulb globe temperature under alternative climate scenarios. *Atmosphere* **9**, 187 (2018).
60. Wang, J. et al. Anthropogenic emissions and urbanization increase risk of compound hot extremes in cities. *Nat. Clim. Change* **11**, 1084 (2021).
61. Chen, B. et al. The evolution of social-ecological system interactions and their impact on the urban thermal environment. *NPJ Urban Sustain.* **4**, 3 (2024).
62. Zhang, J., Ren, G. & You, Q. Detection and attribution of human-perceived warming over China. *Geophys. Res. Lett.* **51**, e2023GL106283 (2024).
63. Kang, S., & Eltahir, E. A. B. North China plain threatened by deadly heatwaves due to climate change and irrigation. *Nat. Commun.* **9**, 2894 (2018).
64. Li, D. & Bou-Zeid, E. Synergistic Interactions between urban heat islands and heat waves: the impact in cities is larger than the sum of its parts*. *J. Appl. Meteorol. Climatol.* **52**, 2051–2064 (2013).
65. Matthews, T. K. R., Wilby, R. L. & Murphy, C. Communicating the deadly consequences of global warming for human heat stress. *Proc. Natl. Acad. Sci. USA* **114**, 3861–3866 (2017).
66. Willett, K. M. & Sherwood, S. Exceedance of heat index thresholds for 15 regions under a warming climate using the wet-bulb globe temperature. *Int. J. Climatol.* **32**, 161–177 (2012).
67. Huang, S. et al. Widespread global exacerbation of extreme drought induced by urbanization. *Nat. Cities* **1**, 597–609 (2024).
68. Tripathi, R. J. & Kumar, D. A holistic approach for solar-driven HVAC evaporative cooling system: comparative study of dry and wet channel. *J. Build. Eng.* **83**, 108465 (2024).
69. Buzan, J. R. & Huber, M. Moist heat stress on a hotter Earth. *Annu. Rev. Earth Planet. Sci.* **48**, 623 (2020).
70. Buzan, J. R., Oleson, K. & Huber, M. Implementation and comparison of a suite of heat stress metrics within the Community Land Model version 4.5. *Geosci. Model Dev.* **8**, 151–170 (2015).
71. Peng, J. et al. Decoupling of temperature and water vapor in terrestrial monsoon regions due to decreasing ocean evaporation at low latitudes. *J. Geophys. Res. Atmos.* **130**, e2024JD042675 (2025).
72. He, Y. Y. et al. Spatial-temporal changes of compound temperature-humidity extremes in humid subtropical high-density cities: an observational study in Hong Kong from 1961 to 2020. *Urban Clim.* **51**, 101669 (2023).
73. Huang, W. T. K. et al. Economic valuation of temperature-related mortality attributed to urban heat islands in European cities. *Nat. Commun.* **14**, 7438 (2023).
74. Sheng, T. Y. et al. Examining urban agglomeration heat island with explainable AI: an enhanced consideration of anthropogenic heat emissions. *Urban Clim.* **59**, 102251 (2025).
75. Speizer, S., Raymond, C., Ivanovich, C. & Horton, R. M. Concentrated and intensifying humid heat extremes in the IPCC AR6 regions. *Geophys. Res. Lett.* **49**, e2021GL097261 (2022).
76. Zhang, J., Ren, G. & You, Q. Assessing the escalating human-perceived heatwaves in a warming world: the case of China. *Weather Clim. Extrem.* **43**, 100643 (2024).
77. Ramsay, E. E. et al. Chronic heat stress in tropical urban informal settlements. *iScience* **24**, 103248 (2021).
78. Mora, C. et al. Global risk of deadly heat. *Nat. Clim. Change* **7**, 501 (2017).
79. Jones, B. & O'Neill, B. C. Spatially explicit global population scenarios consistent with the shared socioeconomic pathways. *Environ. Res. Lett.* **11**, 084003 (2016).
80. Zeng, J. X. et al. Comparison of the risks and drivers of compound hot-dry and hot-wet extremes in a warming world. *Environ. Res. Lett.* **19**, 114026 (2024).
81. Xu, F., Chan, T. O. & Luo, M. Different changes in dry and humid heat waves over China. *Int. J. Climatol.* **41**, 1369–1382 (2021).
82. Fischer, E. M., Sippel, S. & Knutti, R. Increasing probability of record-shattering climate extremes. *Nat. Clim. Change* **11**, 689 (2021).
83. Dong, J. Q., Hu, T., Broennimann, S., Liu, Y. X. & Peng, J. GSDM-WBT: global station-based daily maximum wet-bulb temperature data for 1981-2020. *Earth Syst. Sci. Data* **14**, 5651–5664 (2022).
84. Hersbach, H. et al. The ERA5 global reanalysis. *Q. J. R. Meteorol. Soc.* **146**, 1999–2049 (2020).
85. Liu, L. L., Cao, X., Li, S. J. & Jie, N. A 31-year (1990-2020) global gridded population dataset generated by cluster analysis and statistical learning. *Sci. Data* **11**, 124 (2024).
86. ORNL. *LandScan Global Population Database (2000-2020)* (Oak Ridge National Laboratory, accessed 11 March 2024).
87. Wang, X., Meng, X. & Long, Y. Projecting 1 km-grid population distributions from 2020 to 2100 globally under shared socioeconomic pathways. *Sci. Data* **9**, 563 (2022).
88. Li, M. et al. Spatiotemporally consistent global dataset of the GIMMS normalized difference vegetation index (PKU GIMMS NDVI) from 1982 to 2022. *Earth Syst. Sci. Data* **15**, 4181–4203 (2023).
89. Ajmar, A., Arco, E. & Eusebio, A. The VIIRS nighttime lights average annual global dataset: exploratory and brisk trend analysis on three different domains. In *Proc. 21st IEEE Mediterranean Electrotechnical Conference (IEEE MELECON)*454–459 (IEEE, 2022).
90. Coffel, E. D., Horton, R. M. & de Sherbinin, A. Temperature and humidity based projections of a rapid rise in global heat stress exposure during the 21st century. *Environ. Res. Lett.* **13**, 014001 (2018).
91. Moratiel, R., Soriano, B., Centeno, A., Spano, D. & Snyder, R. L. Wet-bulb, dew point, and air temperature trends in Spain. *Theor. Appl. Climatol.* **130**, 419–434 (2016).
92. Davies-Jones, R. An efficient and accurate method for computing the wet-bulb temperature along pseudoadiabats. *Mon. Weather Rev.* **136**, 2764–2785 (2008).
93. Menne, J. et al. An overview of the global historical climatology network-daily database. *J. Atmos. Ocean. Technol.* **29**, 897–910 (2012).
94. Zhao, N., Zhou, Y. & Samson, E. L. Correcting incompatible DN values and geometric errors in nighttime lights time-series images. *IEEE Trans. Geosci. Remote Sens.* **53**, 2039–2049 (2015).
95. Li, X., Zhou, Y., Zhao, M. & Zhao, X. A harmonized global nighttime light dataset 1992–2018. *Sci. Data* **7**, 168 (2020).


## Acknowledgements

This study is supported by the Major Science and Technology Special Project of Xinjiang Uygur Autonomous Region (grant no.: 2024A03006-2), the Major Demonstration Project for Scientific and Technological Innovation in the Inner Mongolia Autonomous Region (grant no. 2025ZDSF0009-04), and the Research Initiation Project for High-Level Talent Team of Arospace Information Technology University (nos. 301010102 and 301010202).

## Author contributions

L.X., Q.Z., and S.T. designed the research and wrote the manuscript. L.X. performed the analysis. Q.Z., L.X., S.T., H.S., and X.G. discussed and modified the manuscript. All authors contributed to the interpretation of the results.

## Competing interests

The authors declare no competing interests.

## Additional information

**Supplementary information** The online version contains Supplementary material available at https://doi.org/10.1038/s43247-026-03437-8.

**Correspondence** and requests for materials should be addressed to Qiang Zhang.

**Peer review information** *Communications Earth and Environment* thanks Pouya Vahmani and the other anonymous reviewer(s) for their contribution to the peer review of this work. Primary handling editors: Mengze Li and ChenRui Diao. A peer review file is available.

**Reprints and permissions information** is available at http://www.nature.com/reprints

**Publisher's note** Springer Nature remains neutral with regard to jurisdictional claims in published maps and institutional affiliations.

**Open Access** This article is licensed under a Creative Commons Attribution-NonCommercial-NoDerivatives 4.0 International License, which permits any non-commercial use, sharing, distribution and reproduction in any medium or format, as long as you give appropriate credit to the original author(s) and the source, provide a link to the Creative Commons licence, and indicate if you modified the licensed material. You do not have permission under this licence to share adapted material derived from this article or parts of it. The images or other third party material in this article are included in the article's Creative Commons licence, unless indicated otherwise in a credit line to the material. If material is not included in the article's Creative Commons licence and your intended use is not permitted by statutory regulation or exceeds the permitted use, you will need to obtain permission directly from the copyright holder. To view a copy of this licence, visit http://creativecommons.org/licenses/by-nc-nd/4.0/.

© The Author(s) 2026